

MANIBOX: ENHANCING SPATIAL GRASPING GENERALIZATION VIA SCALABLE SIMULATION DATA GENERATION

Hengkai Tan^{1*}, Xuezhou Xu^{2*}, Chengyang Ying¹, Xinyi Mao¹, Songming Liu¹,
Xingxing Zhang¹, Hang Su¹, Jun Zhu¹

¹Tsinghua University ²National University of Singapore

ABSTRACT

Learning a precise robotic grasping policy is crucial for embodied agents operating in complex real-world manipulation tasks. Despite significant advancements, most models still struggle with accurate spatial positioning of objects to be grasped. We first show that this spatial generalization challenge stems primarily from the extensive data requirements for adequate spatial understanding. However, collecting such data with real robots is prohibitively expensive, and relying on simulation data often leads to visual generalization gaps upon deployment. To overcome these challenges, we then focus on state-based policy generalization and present **ManiBox**, a novel bounding-box-guided manipulation method built on a simulation-based teacher-student framework. The teacher policy efficiently generates scalable simulation data using bounding boxes, which are proven to uniquely determine the objects’ spatial positions. The student policy then utilizes these low-dimensional spatial states to enable zero-shot transfer to real robots. Through comprehensive evaluations in simulated and real-world environments, ManiBox demonstrates a marked improvement in spatial grasping generalization and adaptability to diverse objects and backgrounds. Further, our empirical study into scaling laws for policy performance indicates that spatial volume generalization scales positively with data volume. For a certain level of spatial volume, the success rate of grasping empirically follows Michaelis-Menten kinetics relative to data volume, showing a saturation effect as data increases. Our videos and code are available in the [project page](#).

1 INTRODUCTION

Robotic manipulation in dynamic environments is pivotal for advancing modern robotics (Fu et al., 2024). Equipping robots with precise grasping capabilities in unstructured settings not only extends their utility beyond traditional static scenarios but also enhances their real-world effectiveness, especially in industrial and domestic settings. A robot policy that achieves **spatial generalization**—defined as the ability of a manipulation model to complete tasks regardless of the target object’s position within a defined spatial volume—would be particularly practical. Such generalization is vital when deploying robots in diverse environments, such as different households, where they must handle various objects on different platforms. The capability to perform successfully across these varied spatial conditions is essential, as objects in real-world settings are rarely fixed in place, and effective manipulation demands adaptability to a broad range of spatial challenges.

Recent works have made notable progress in robotic manipulation in multi-task and multi-environment scenarios, which is largely driven by end-to-end training methodologies (Ahn et al., 2022; Shridhar et al., 2022; 2023; Zitkovich et al., 2023). Notably, some large embodied foundation models for manipulation, such as those fine-tuned from Vision-Language Models (VLMs) for multi-task robot manipulation tasks (Brohan et al., 2022; Kim et al., 2024), have made significant strides. However, these large manipulation models derived from VLMs often lack sufficient spatial awareness and reasoning capabilities, posing substantial challenges for large-scale spatial generalization in real-world applications (Cheng et al., 2024a). Our analysis in Lemma 1 suggests that achieving

*Equal contribution

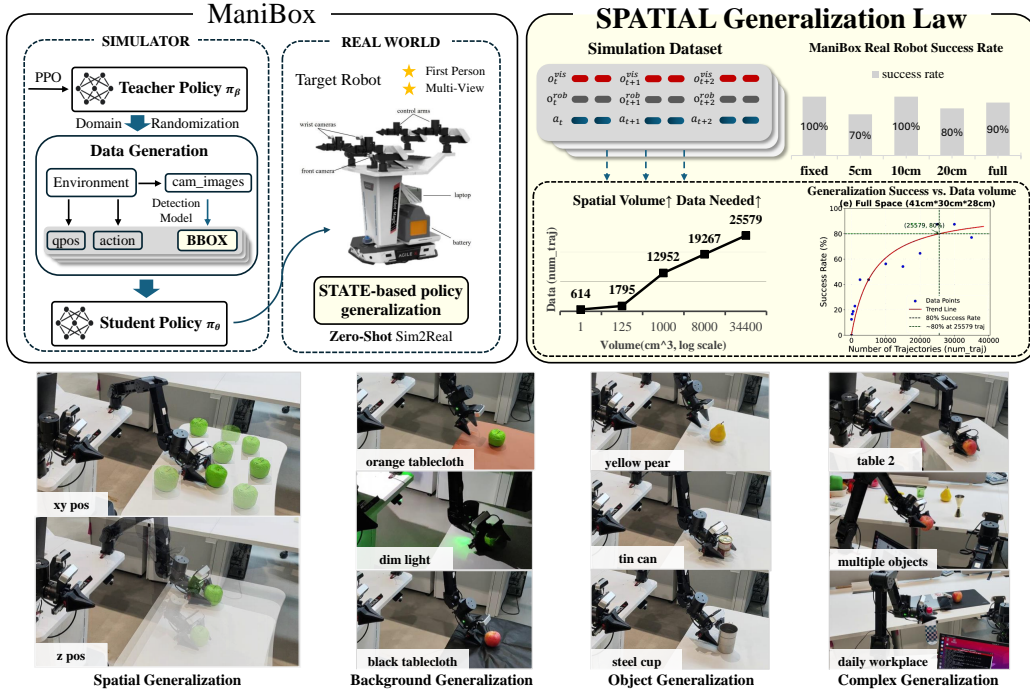


Figure 1: **Overview.** We introduce ManiBox, a bbox-guided manipulation method using a teacher-student framework to enhance spatial generalization in grasping policies. We reveal that spatial volume generalization scales positively with data volume, with grasping success following Michaelis-Menten kinetics relative to data volume for specified spatial volumes. Extensive real-world tests show ManiBox’s robust adaptability to varied spatial positions, objects, and backgrounds.

spatial generalization over larger volumes requires substantially more data, a relationship we further empirically verify to follow a positive scaling law (see Figure 4). For example, training a model to grasp at a fixed point may require only 50 to 600 trajectory datasets. However, when generalizing the model to operate within a spatial volume of $34,400\text{cm}^3$ ($41\text{cm} \times 30\text{cm} \times 28\text{cm}$), which approximates the maximum reach of our robotic arm, the data requirement increases by roughly 40-fold, demanding tens of thousands of trajectories

However, collecting such a large volume of data on real robots is prohibitively expensive. For instance, RT-1 required 17 months to accumulate 130K episodes (Brohan et al., 2022), which is a level of resource commitment unfeasible for most research labs. Although simulation data can help bridge this gap, significant high-dimensional visual discrepancies between simulated and real environments, known as the Sim2Real gap, pose additional challenges. While prior efforts have aimed to enhance performance using various visual generalization techniques, each method comes with its drawbacks. Some demand unobstructed third-person perspectives (Yuan et al., 2024), some consume substantial computational resources (Shridhar et al., 2023; Ahn et al., 2022). These requirements can impede real-time processing and practical deployment on resource-limited robotic platforms.

While perception models are essential for object and environmental recognition, the true effectiveness of a robot in dynamic settings hinges on the robustness of its policy execution. A well-generalized policy empowers the robot to autonomously adjust its actions in real-time, effectively compensating for visual inaccuracies and adapting to changes in object positions or environmental dynamics. Such adaptability is crucial for achieving task success and maintaining system stability, especially in the face of imperfect or noisy perception data. To further enhance the robot’s ability to manage unpredictable scenarios and ensure reliable real-world performance, we shift our focus to **state-based policy generalization** instead of relying solely on vision-based methods. Our Lemma 2 demonstrates that bounding boxes, when captured from multiple cameras, effectively encapsulate the 3D structure of convex objects, providing an optimal low-dimensional state for policy generalization. Building on this foundation, we introduce a novel bounding-box-guided methodology **ManiBox** to enhance spatial generalization and adaptability.

In the simulator, ManiBox utilizes reinforcement learning (RL) with privileged information to train a sophisticated teacher policy. This policy generates scalable robot trajectory data, replacing traditional visual inputs with bounding box coordinates to facilitate spatial generalization of grasping policies. Subsequently, the student policy, trained on this simulation data, achieves robust zero-shot transfer to real-world tasks, leveraging bounding boxes identified by advanced open-vocabulary detection models, such as YOLO-World (Cheng et al., 2024b). Extensive experiments with both simulators and real robots demonstrate a direct correlation between data volume and spatial generalization performance: *more data consistently leads to higher grasping success rates, and generalizing to larger spatial volumes requires even more data*. For instance, to reliably grasp objects within a 1000cm^3 workspace, tens of thousands of trajectories from various positions are required. ManiBox achieves nearly perfect success rates in real-world grasping tasks by leveraging large-scale simulation data generated across diverse spatial volumes. Furthermore, ManiBox exhibits robust generalization, successfully grasping objects in new scenarios, including unfamiliar object types, complex surfaces, changing lighting conditions, and environments with distractions.

Our contributions include: (1) We introduce **ManiBox**, an innovative bounding-box-guided manipulation method that addresses the limitations of visual generalization, offering a robust solution for spatial generalization in grasping tasks; (2) ManiBox significantly enhances adaptability to diverse spatial positions, object types, and backgrounds, as demonstrated by extensive experiments in both simulated and real-world environments; (3) Through scalable simulation data generation, we provide novel insights into the relationship between data volume and spatial generalization, establishing a framework for improving generalization across a variety of embodied systems.

2 RELATED WORK

Learning from Simulation. Simulators provide an efficient and scalable way to expand embodiment datasets, offering a cost-effective means for parallel data collection and faster iteration cycles. There are three main approaches for leveraging simulation in robotic control: 1) training reinforcement learning (RL) agents through interaction within the simulator (Huang et al., 2023; Radosavovic et al., 2024; Yuan et al., 2024), 2) using imitation learning based on expert demonstrations generated in simulation (Xie et al., 2020; Tan et al., 2024), and 3) employing a teacher-student framework, where privileged information from simulation trains a teacher policy to guide a student policy (Lee et al., 2020a; Geng et al., 2023; Zhuang et al., 2023), as demonstrated in the ManiBox framework. These methods reduce the reliance on expensive real-world data collection.

Various techniques have been developed to bridge the Sim2Real gap, including realistic simulators (Todorov et al., 2012; James et al., 2020; Makoviychuk et al., 2021), domain randomization (Tobin et al., 2017; Peng et al., 2018; Zhuang et al., 2023), and vision-based policy generalization (Geng et al., 2023; Tan et al., 2024; Ying et al., 2024; Yuan et al., 2024). These approaches enable robots to generalize across diverse visual and physical conditions, which are critical in real-world environments. For example, domain randomization allows policies trained in varied simulated conditions to transfer effectively to real-world scenarios (Tobin et al., 2017; Peng et al., 2018). While real-world datasets such as Open X-Embodiment (Padalkar et al., 2023) provide 1M demonstrations, they are much smaller than datasets in other domains like language and images (Lehmann et al., 2015; Mühleisen & Bizer, 2012; Weyand et al., 2020; Wu et al., 2019). Thus, simulation-generated datasets play a vital role in compensating for the limitations of real-world data collection.

Visual Generalization for Robotic Manipulation. Visual generalization is fundamental for robotic manipulation in dynamic environments, where robots must handle varying visual inputs and changing conditions, such as object positions and lighting variations. Vision-based policy generalization, which leverages both simulated and real-world data, addresses these challenges. By simulating diverse visual scenarios, robots can better generalize to new environments and tasks. For instance, multi-task and multi-object manipulation studies have extended behavior cloning to handle a wide range of visual inputs, improving generalization to unseen objects and scenes (Vuong et al., 2023; Fang et al., 2023). Additionally, language-conditioned policies (Brohan et al., 2022; Zitkovich et al., 2023; Shridhar et al., 2023) and imitation learning from human videos (Chen et al., 2021; Nair et al., 2023) enable robots to interpret and manipulate objects using both visual and language cues.

However, scaling real-world demonstrations to improve generalization remains challenging due to resource constraints. Simulation-based learning mitigates this by offering large, diverse visual data.

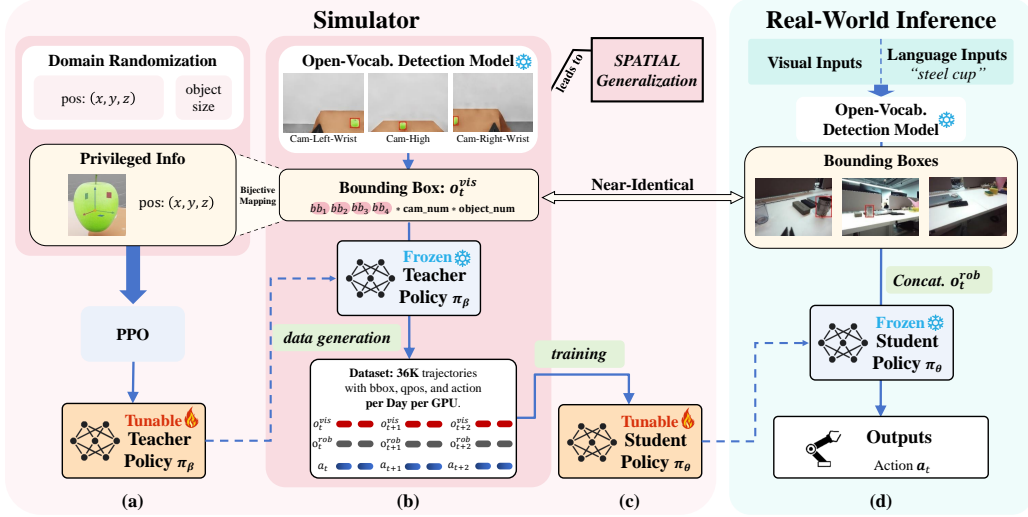


Figure 2: **ManiBox illustration.** (a) Utilizing PPO and domain randomization, we train a sophisticated teacher policy in the simulator that utilizes privileged object information to determine actions. (b) The teacher policy generates scalable trajectory data, utilizing bounding box coordinates instead of traditional high-dimensional visual inputs or privileged information. (c) A state-based student policy, generalizable and capable of zero-shot transfer, is trained on this extensive simulation dataset, greatly improving spatial generalization. (d) Guided by bounding boxes, the student policy precisely executes actions for real robots, achieving improved generalization capabilities.

Domain randomization techniques (Tobin et al., 2017; Peng et al., 2018) have proven effective in generating varied visual conditions, enabling models to generalize more robustly across real-world tasks. While methods like bounding box annotations assist in specific tasks such as pose estimation (Huang et al., 2023), understanding the relationship between dataset scale and generalization remains an area that requires further exploration. As simulation data grows, more research is needed to evaluate how data volume impacts policy generalization, particularly in dynamic environments.

3 METHODOLOGY

In this section, we first formulate the problem and then introduce our method ManiBox, including the teacher policy training, simulation data generalization, and student policy distillation.

3.1 PROBLEM FORMULATION

For robotic manipulation, especially within dynamic environments, achieving spatial generalization (i.e., the ability to effectively perform tasks across varied spatial configurations) is essential for usability and overall efficacy. We formulate robotic manipulation as a partially observable Markov decision process (POMDP) (Cassandra et al., 1994), by considering the robot’s limited access to complete state information, the necessity to make decisions under uncertainty, as well as the inherently stochastic nature of its interactions with the environment. Formally, the decision-making process is characterized by the tuple $\mathcal{M} = (\mathcal{S}, \mathcal{A}, \mathcal{O}, \mathcal{T}, \mathcal{R}, \gamma)$, where \mathcal{S} represents the state space, including all configurations of the robot and its environment; \mathcal{A} denotes the action space, containing all possible robot actions; \mathcal{O} is the observation space, which reflects the limited state information accessible to the robot; \mathcal{T} defines the state transition dynamics, $\mathcal{T}(s_{t+1}|s_t, a_t)$; \mathcal{R} is the reward function, providing feedback based on the state-action pair $\mathcal{R}(s_t, a_t)$; and γ is the discount factor.

In real-world scenarios, the robot receives partial observations $o_t \in \mathcal{O}$ through an observation function, which provides incomplete and potentially noisy information about the true state s_t . The observation can be represented as $o_t \sim \mathcal{O}(s_t)$. The robot’s objective is to find a policy π that maps observations (or histories of observations) to actions $a_t \sim \pi(a_t|\tau_t)$, where $\tau_t = (o_0, a_0, o_1, a_1, \dots, o_t)$ is the history up to time t . The policy is expected to maximize the expected cumulative reward:

$$J(\pi) = \mathbb{E}_\pi \left[\sum_{t=0}^{\infty} \gamma^t \mathcal{R}(s_t, a_t) \right], \quad (1)$$

where the expectation is over the trajectories induced by the policy π . However, solving POMDPs for manipulation tasks is computationally expensive, as it requires maintaining a belief distribution over all possible states, including the precise position, orientation, and object dynamics. This complexity is compounded by the need to handle occlusions, sensor noise, and dynamic changes in the environment, making it challenging for robots to operate efficiently in real-world settings where the state is constantly evolving and uncertain (Kaelbling et al., 1998; Kochenderfer, 2015).

To reduce this complexity and ensure Sim2Real transfer, we adopt a widely used teacher-student framework (Lee et al., 2020a; Geng et al., 2023), building upon which, we develop **ManiBox**, a novel bounding-box-guided manipulation method that offers significant advantages in spatial generalization over vision-based RL methods. First, ManiBox enables efficient, scalable data generation, as the teacher policy in simulation can produce a large and diverse set of trajectories. Additionally, by using low-dimensional bounding box states, the state-based student policy can accelerate learning and effectively transfer from simulation to the real world.

However, this framework also faces notable challenges. The teacher policy must efficiently explore a high-dimensional state space in simulation, which can be computationally intensive. The student policy must derive optimal actions from incomplete observations and adjust to real-world variations such as sensor noise and dynamic environmental conditions not present in simulations. Detailed strategies for overcoming these challenges are discussed in the following sections.

3.2 TEACHER POLICY TRAINING

To automatically and efficiently generate a large amounts of diverse data, we first train an expert teacher policy $\pi_\beta : \mathcal{S} \rightarrow \mathcal{A}$ using RL, as the expert data generator. The **teacher policy** $\pi_\beta(\mathbf{a}_t | \mathbf{s}_t)$ is trained in a simulated environment where it has access to full state information \mathbf{s}_t , including privileged information such as precise object positions. The teacher policy is optimized using reinforcement learning (RL) to maximize the expected reward:

$$J_\beta = \mathbb{E}_{\pi_\beta} \left[\sum_{t=0}^{\infty} \gamma^t \mathcal{R}(\mathbf{s}_t, \mathbf{a}_t) \right], \quad (2)$$

where the reward function is defined to guide the policy in grasping the object and moving it to a specified location. We select the grasping task to validate our approach’s core concept. This allows the teacher to generate a diverse set of optimal trajectories across a wide range of spatial configurations. These trajectories serve as training data for the student policy, guiding it to learn effective manipulation policies.

However, due to challenges such as the high dimensionality of the state space and the large exploration space caused by the multi-stage reward function during the training of the teacher policy, the number of samples required for RL training is significantly large. Therefore, in addition to optimizing the policy using the Proximal Policy Optimization (PPO) (Schulman et al., 2017) algorithm, we also make adjustments to the RL environment to reduce the exploration space and make it easier for the policy π_β to find the point with the highest return (More details are in Appendix C.1):

Environment Setup. To ensure efficient data generation and policy training, we utilize Isaac Lab (Mittal et al., 2023), which supports large-scale parallelism environments. The scene includes basic elements like a platform, objects, and a robot, arranged simply to facilitate future domain randomization. The robot’s goal is to grasp the object on the table and move it to a designated location. We integrate the dual-arm Mobile ALOHA (Fu et al., 2024) robot, equipped with three first-person view RGB cameras, into the simulator and ensure its dynamics are consistent with the real world.

State. For training efficiency, our teacher policy is state-based and can access full state information \mathbf{s}_t . As the robot lacks visual input, we include privileged information like the object’s position in the state information. The privileged information accelerates RL training and enables the agent to learn more efficient and generalized policies.

Domain Randomization. To improve the generalization of the teacher policy and enhance the spatial diversity of the generated data, we adopt several domain randomization techniques:

- *objective position* (x, y, z): To generalize the grasping policy to the whole space, we apply the domain randomization for all three dimensions of x , y , and z , ensuring that the x -coordinate and y -coordinate of the object, which is chosen randomly, can cover a large

range. Moreover, the height of the platform is randomized to ensure that the z-coordinate of the object in the data can cover the feasible working space of the robotic arm.

- *object size*: To ensure that the grasping policy covers objects of *various sizes*, the size of the object is also randomized.

These two domain randomization techniques allow teacher policy can grasp different objects of different positions and sizes, which is significant for real-world generalization. By combining privileged information and domain randomization, the teacher policy can efficiently generate a large amount of diverse data to achieve spatial generalization.

3.3 SIMULATION DATA GENERATION

We utilize the teacher policy to automatically generate data for training a student policy that can be deployed in the real world across different objects, grasping spatial positions, and backgrounds.

Data Volume Estimation. To guide the data volume needed for policy generalization to a specific spatial volume, we now analyze the sample efficiency for generalizing in a $b \times b \times b$ cube. Based on the classical learning theory, the sample complexity of uniform convergence property is in proportion to the VC dimension of the model hypothesis set (Shalev-Shwartz & Ben-David, 2014). Extending previous results about generalization bounds for multi-task learning (Crammer & Mansour, 2012), we can have the following results:

Lemma 1 (Details are in Appendix A.1). *For training a grasp agent that can generalize spatially within a cube whose size is $b \times b \times b$ via imitation learning, under some mild assumptions in Crammer & Mansour (2012), the VC dimension is at most proportional to $d \log(Cb^3d)$, where d is the VC dimension of the hypothesis set for grasping the fixed point and C is a constant independent of d, b .*

This lemma demonstrates that the data required for policy generalization to a certain volume grows, thus it is necessary to collect data from the simulator. This result gives us a rough estimation of how much data we need to collect with the increasing of the spatial cube needs to generalize.

In light of this Lemma 1, we need a large scale of trajectories to train a student policy feasible under full spatial range. This calls for conciseness in data generation and collection, otherwise it will place a heavy burden on student policy training. On the other hand, since the teacher policy trained with privileged information (i.e. object positions) cannot directly transfer from simulation to reality (Sim2Real), the student policy needs visual observations that implicitly encode object position information. However, there remains a significant Sim2Real gap between visual images in the simulator and those in the real world because the vast complexity of real-world environments cannot be fully simulated by the simulator (e.g. various backgrounds and objects). Additionally, vision-based policy is difficult to train on a large scale and requires data augmentation.

To address this Sim2Real gap and enable robust spatial generalization, we propose using an individual vision module to extract the bounding box from camera views as a **consistent, low-dimensional, and complete** representation of the object’s spatial properties, such as position and size.

Using Bounding Boxes to Provide Complete 3D Information about the Object. To efficiently generate a large amount of simulator data that aligns with real-world visual images, the vision module must be robust, mature, and efficient. Considering open-vocabulary detection, we selected YOLO-World (Cheng et al., 2024b) as the frozen 2D visual feature extraction module. This provides us with the bounding box of the objects as the 2D low-dimensional visual feature, which is consistent and low-dimensional. Notably, the inference time of YOLO-World for a single image is around 30ms, ensuring the data generalization efficiency and real-time inference in the real world.

In addition, to ensure that these multi-view 2D low-dimensional visual features can offer complete information about object position and size, we present a lemma: Suppose the object is a sphere, the 3D information of the object can be uniquely determined by the bounding boxes from two cameras:

Lemma 2 (Details and proofs are in Appendix A.2). *Given: (1) Two pinhole cameras with known intrinsic parameters K_i and extrinsic parameters (R_i, t_i) ; (2) A sphere of unknown radius r is fully visible in both camera images without occlusion; (3) Normalized image coordinates of the bounding boxes of the sphere in both images: Camera i : $(u_{i\min}, v_{i\min}, u_{i\max}, v_{i\max})$, the image dimensions are known (width W_i and height H_i for each camera).*

Then the 3D coordinates of the sphere’s center C in the world coordinate system and the radius r of the sphere can be uniquely determined using the known camera parameters, and the normalized bounding box coordinates, provided that the cameras are not in degenerate configurations.

This lemma illustrates that 3D position information of a sphere can be implied by utilizing multi-view bounding boxes, indicating our ManiBox can capture complete spatial position information of target objects for real-world control policies.

In short, our approach of using an individual vision module simplifies the transition from simulation to the real world by providing the student policy with consistent inputs across both domains. Specifically, the student policy receives both proprioceptive data $\mathbf{o}_t^{\text{rob}}$ and bounding box data $\mathbf{o}_t^{\text{vis}}$ as inputs:

$$\pi_\theta : \mathcal{O} = \mathcal{O}_{\text{rob}} \times \mathcal{O}_{\text{vis}} \rightarrow \mathcal{A}. \quad (3)$$

3.4 STUDENT POLICY DISTILLATION

While the teacher policy and data generation are completed in the simulator, the student policy is deployed on a real robot and relies only on partial observations in the real world. The student policy needs to ensure high generalizability in real-world environments. Consequently, real-world variations, such as sensor noise and dynamic environments, pose challenges not encountered in the simulation environment to our student policy. For instance, an open-vocabulary detection model (namely YOLO-World (Cheng et al., 2024b) in our practice) can fail to recognize real-world target objects at times because of background distraction or robot gripper occlusion, while the recognition of the simulated target object rarely fails.

In this context, we introduce the random mask to bridge this sim-to-real gap and further improve the robustness of our policy. In detail, when distilling our student policy from the simulation data \mathcal{D} , for each trajectory, we randomly mask some bboxes (i.e., set them to 0) with a probability pre-defined as `random_mask_ratio`, indicating that this camera does not recognize the target object. This approach replicates the real-world scenarios where the open-vocabulary detection model fails to generate the bounding box.

On top of this expected unpredictable failure and partial observability, our policy requires encoding sufficient history information (Hafner et al., 2019; Lee et al., 2020b; Ying et al., 2023). For this reason, we use RNN for our student policy:

$$\begin{aligned} \mathbf{x}_t, \mathbf{h}_t &= \text{LSTM}(\mathbf{s}'_t, \mathbf{h}_{t-1}), \\ \mathbf{a}_t &= \text{FC}_2(\text{drop}(\text{gelu}(\text{FC}_1(\mathbf{x}_t))))), \end{aligned} \quad (4)$$

where $\text{LSTM}(\cdot)$, $\text{gelu}(\cdot)$, $\text{drop}(\cdot)$, $\text{FC}(\cdot)$ represent the Long Short-Term Memory (LSTM) (Hochreiter & Schmidhuber, 1997), Gaussian Error Linear Unit (GELU) activation (Hendrycks & Gimpel, 2016), dropout (Srivastava et al., 2014), and Fully Connected layer (FC) respectively.

This combination of random mask and trajectory modeling significantly contributes to the robustness and generalization of our student policy in deployment, conquering the challenge of partial observations and unseen real-world variations.

4 EXPERIMENTS

In this section, we conduct extensive experiments in both the simulator and the real world, covering various random backgrounds, objects, and positions to answer the following questions: (1) What is the scaling relationship between spatial generalization and data amounts in the grasping task? (Sec. 4.2) and (2) What about the efficacy of our method, especially its generalization ability to different backgrounds, objects, and object spatial positions in real-world applications? (Sec. 4.3)

4.1 EXPERIMENTAL SETUP

Tasks. To validate the generalization of Manibox, we test our approach under the grasping task. In the simulator, the articulated arm and end effector are required to pick up a green apple randomly placed on a table in a $41\text{cm} * 30\text{cm} * 28\text{cm}$ (length*width*height) spatial scale, which is referred to as "Full Space." Also, real-world counterparts are established with alternative objects, backgrounds,

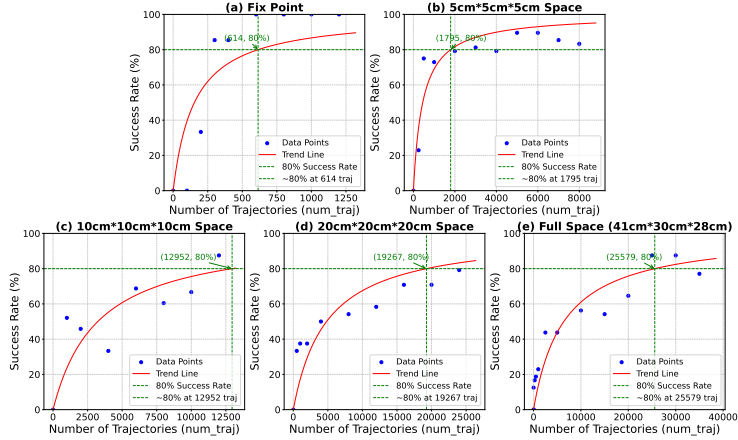


Figure 3: The scaling relationship between spatial generalization and data amounts under different spatial ranges in the grasping task. The data volume is the number of trajectories used for training the student policy. The estimated point with an 80% success rate is annotated additionally.

and settings to further demonstrate the generalization ability. In both scenarios, three RGB images taken by wrist cameras and the exterior camera are taken as observations.

Real Robot. Mobile ALOHA (Fu et al., 2024) is a cost-effective and highly stable robot designed for both data collection and manipulation tasks. It owns four arms: two for teleoperation during data collection and two subordinate arms that perform manipulation tasks. Each subordinate arm is fitted with an RGB camera on its wrist, complemented by another RGB camera centrally mounted on the robot’s body. Mobile ALOHA has demonstrated strong generalization capabilities across a diverse range of complex grasping tasks, making it an ideal choice for implementing our student policy.

4.2 SPATIAL SCALING LAW WITH DATA

To guide us in determining the data volume required for a certain level of spatial generalization, we investigate the relationship between policy performance and data volume. We conduct extensive experiments in the simulator to evaluate the success rate of policies trained on different data volumes. We select five distinct spatial ranges to explore this scaling behavior, including one fixed range and four dynamic ranges of 5, 10, 20 units, and full space. For each spatial range, we select more than 8 data volumes to train the student policy and evaluate its grasping success rate at random positions.

The results shown in Fig. 3 demonstrate that a scaling law holds in this context: For each spatial range, the pattern is as follows: when the data volume is zero, the policy inevitably fails. As the data volume increases, the success rate of the grasping policy improves, but the growth slows down. Eventually, the success rate surpasses 80% and tends to 100%.

Furthermore, we identify the data volume required to achieve an 80% success rate for each spatial range (as shown in Fig. 3) and find that the volume of the spatial range and the required data follow a power rate relationship (as shown in Fig. 4).

The positive correlation between data volume and spatial volume provides guidance for data-driven spatial generalization: The more data we have, the higher the robot’s manipulation success rate. As the spatial range increases, more data is required, and the data volume needed grows with the space volume as a power rate relationship. In fact, for the same task, achieving high generalization success over a $41cm * 30cm * 28cm = 34440cm^3$ range may require at least 20,000 trajectory data from different spatial positions. Such large-scale data

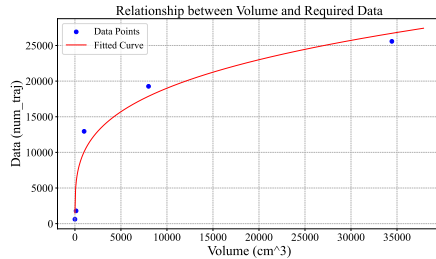


Figure 4: The relationship between spatial volume and data amounts needed to reach 80% grasping success rate. The fitted curve represents a power function of $y = 1507 \cdot x^{0.28}$.

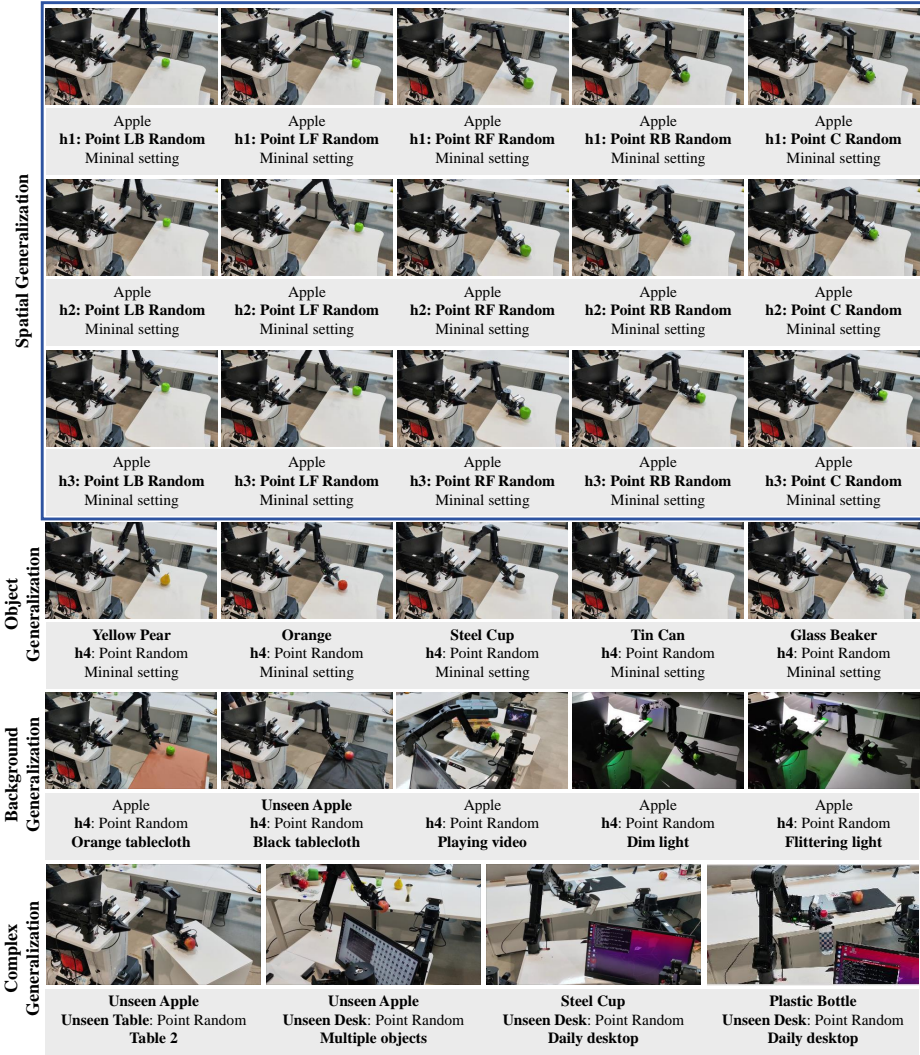


Figure 5: Demonstration of the generalization of our methods across different backgrounds, objects, and positions. The h1, h2, h3, h4 are randomly selected object heights in the real world, which are approximately 57cm, 65cm, 72cm, and 65cm. LB, LF, RF, RB, and C are abbreviations for Left-Back, Left-Front, Right-Front, Right-Back, and Center area respectively.

collection would be expensive in the real world, making simulator-generated data a more affordable and efficient option. This further emphasizes the significance of simulation data.

To further demonstrate the importance of other variables (e.g. time) in spatial intelligence and the robustness of policy generalization to visual uncertainty, we have further discussion on the spatial intelligence of our policy through detailed ablation experiments. Details are provided in Appendix B.

4.3 REAL-WORLD RESULTS

To validate the generalization ability of our method and policy in the real world, we compare the success rate of our policy with the vision-based ACT. In practice, we deploy models trained on simulation data onto a real robot and test their performance on grasping tasks across multiple arbitrarily chosen positions, eight objects (with some of them out-of-distribution), five backgrounds, and three unseen settings as illustrated in Figure 5. More images and videos of these tests are in the Appendix E.3 and supplementary materials.

Spatial generalization. To justify the efficacy of our method, we assess the generalization capability of our student policy across four spatial ranges and a fixed point. For each experiment, we

randomly place an apple, different from its counterpart in the simulator in both shape and material, on the table at arbitrarily chosen heights within the given range (as illustrated in the first three rows of Fig. 5). Alongside the difference in form and appearance, the apple presents considerable unpredictability to the visual detection model due to factors including background, lighting, target object, etc. Consequently, the bounding box varies in size or even disappears at times, emphasizing the need for robustness in the policy. As shown in Tab. 1, our policy generalizes well to objects falling in different spatial volumes, achieving a success rate between 70% and 100%. In contrast, vision-based ACT, which trains the student policy with the vision input ACT (Zhao et al., 2023), experiences a visible drop on success rate when spatial range scales up, despite its considerable success rate of 70% on a fixed point. The wanting performance of the baseline further demonstrates the significance and necessity of exploring spatial generalization. The results demonstrate that our method harbors strong generalization when addressing uncertainties arising from real-world objects, variations in spatial positions, and visual detection interferences.

Object generalization.

In addition, to justify the object generalization ability of our method, we test our model across eight objects including original apple, unseen apple, yellow pear, orange, steel cup, tin can, glass beaker, and plastic bottle at arbitrarily selected positions. For each unseen object, feeding the corresponding name as a supplement into

Table 1: The real-world success rate of our method and vision-based ACT under varied spatial volumes. We select an approximate data amount based on the results in Fig. 3.

SPATIAL RANGE	METHODS	SUCCESS RATE
Fix Point	Vision-Based ACT	70%
	ManiBox (Ours)	100%
5cm*5cm*5cm	Vision-Based ACT	0%
	ManiBox (Ours)	70%
10cm*10cm*10cm	Vision-Based ACT	0%
	ManiBox (Ours)	100%
20cm*20cm*20cm	Vision-Based ACT	-
	ManiBox (Ours)	80%
Full Space (41cm*30cm*28cm)	Vision-Based ACT	-
	Vision-Based ACT (100 real-world data)	0%
	ManiBox (Ours)	90%

the open-vocabulary visual detection model is enough for the policy to grasp the target object. It is worth noting that two of the objects chosen are out-of-distribution (their bounding boxes are unseen in the simulation data) in an attempt to further illustrate the object generalization ability of our method. This certain level of generalization observed, even when there is significant variation in the bounding box, aligns with our Lemma 2, which proves that the 3D position information of the object is complete in the dataset.

Background Generalization.

Utilizing the strong open-vocab detection ability of YOLO-World, ManiBox can handle various backgrounds and vision disruptions without intentionally varied visual domain randomization. To verify this ability, we experiment with tables of three different shapes and tablecloths in two colors under the minimal setting of a table, an object, and a robot. In addition, we alter the lighting conditions by employing a single stationary point light source and a single flickering point light, as well as playing videos in the background as distractions. Furthermore, we construct two more complex scenarios, one representing a multi-object environment and the other replicating a typical daily workplace desktop. The results demonstrate the strong background generalization ability of our policy. Even though the visual detection model occasionally makes mistakes, the generalization of our policy compensates for those errors. This can be attributed to our policy’s endeavor to integrate historical information, multi-camera data, and random masking to increase the visual model’s tolerance for errors.

5 CONCLUSION

In this work, we present ManiBox, a novel bbox-guided manipulation method, using a simulation-based teacher-student framework to enhance the spatial generalization of grasping policies. To address the challenge of the generalization gap in vision-based models from simulation to real-world deployment, we propose a generalizable, state-based student policy that is innovatively equipped with bbox positions. This policy is trained on scalable simulation data generated by the teacher policy. Extensive experiments in both simulated and real-world environments demonstrate that ManiBox significantly outperforms existing methods in adapting to diverse spatial positions, object configurations, and background variations. Moreover, our theoretical and empirical analyses reveal that the generalization of spatial volume scales positively with the data volume, and the suc-

cess rate follows Michaelis-Menten kinetics for specified spatial volumes. These findings pave the way for the development of robust spatial generalization across a wide range of embodied systems.

REFERENCES

- Michael Ahn, Anthony Brohan, Noah Brown, Yevgen Chebotar, Omar Cortes, Byron David, Chelsea Finn, Chuyuan Fu, Keerthana Gopalakrishnan, Karol Hausman, et al. Do as i can, not as i say: Grounding language in robotic affordances. *arXiv preprint arXiv:2204.01691*, 2022.
- Anthony Brohan, Noah Brown, Justice Carbajal, Yevgen Chebotar, Joseph Dabis, Chelsea Finn, Keerthana Gopalakrishnan, Karol Hausman, Alex Herzog, Jasmine Hsu, et al. Rt-1: Robotics transformer for real-world control at scale. *arXiv preprint arXiv:2212.06817*, 2022.
- Anthony R Cassandra, Leslie Pack Kaelbling, and Michael L Littman. Acting optimally in partially observable stochastic domains. In *Aaai*, volume 94, pp. 1023–1028, 1994.
- Annie S Chen, Suraj Nair, and Chelsea Finn. Learning generalizable robotic reward functions from” in-the-wild” human videos. *arXiv preprint arXiv:2103.16817*, 2021.
- An-Chieh Cheng, Hongxu Yin, Yang Fu, Qiushan Guo, Ruihan Yang, Jan Kautz, Xiaolong Wang, and Sifei Liu. Spatialrgpt: Grounded spatial reasoning in vision language model, 2024a. URL <https://arxiv.org/abs/2406.01584>.
- Tianheng Cheng, Lin Song, Yixiao Ge, Wenyu Liu, Xinggang Wang, and Ying Shan. Yolo-world: Real-time open-vocabulary object detection. In *Proceedings of the IEEE/CVF Conference on Computer Vision and Pattern Recognition*, pp. 16901–16911, 2024b.
- Koby Crammer and Yishay Mansour. Learning multiple tasks using shared hypotheses. *Advances in Neural Information Processing Systems*, 25, 2012.
- Hao-Shu Fang, Chenxi Wang, Hongjie Fang, Minghao Gou, Jirong Liu, Hengxu Yan, Wenhai Liu, Yichen Xie, and Cewu Lu. Anygrasp: Robust and efficient grasp perception in spatial and temporal domains. *IEEE Transactions on Robotics*, 2023.
- Zipeng Fu, Tony Z Zhao, and Chelsea Finn. Mobile aloha: Learning bimanual mobile manipulation with low-cost whole-body teleoperation. *arXiv preprint arXiv:2401.02117*, 2024.
- Haoran Geng, Ziming Li, Yiran Geng, Jiayi Chen, Hao Dong, and He Wang. Partmanip: Learning cross-category generalizable part manipulation policy from point cloud observations. In *Proceedings of the IEEE/CVF Conference on Computer Vision and Pattern Recognition*, pp. 2978–2988, 2023.
- Danijar Hafner, Timothy Lillicrap, Jimmy Ba, and Mohammad Norouzi. Dream to control: Learning behaviors by latent imagination. *arXiv preprint arXiv:1912.01603*, 2019.
- Dan Hendrycks and Kevin Gimpel. Gaussian error linear units (gelus). *arXiv preprint arXiv:1606.08415*, 2016.
- Sepp Hochreiter and Jürgen Schmidhuber. Long short-term memory. *Neural Computation*, 9(8): 1735–1780, 1997.
- Baichuan Huang, Jingjin Yu, and Siddharth Jain. Earl: Eye-on-hand reinforcement learner for dynamic grasping with active pose estimation. In *2023 IEEE/RSJ International Conference on Intelligent Robots and Systems (IROS)*, pp. 2963–2970. IEEE, 2023.
- Stephen James, Zicong Ma, David Rovick Arrojo, and Edward Johns. Rlbench: The robot learning benchmark & learning environment. *IEEE Robotics and Automation Letters (RA-L)*, 5(2):3019–3026, 2020.
- Leslie Pack Kaelbling, Michael L Littman, and Anthony R Cassandra. Planning and acting in partially observable stochastic domains. *Artificial intelligence*, 101(1-2):99–134, 1998.
- Moo Jin Kim, Karl Pertsch, Siddharth Karamcheti, Ted Xiao, Ashwin Balakrishna, Suraj Nair, Rafael Rafailov, Ethan Foster, Grace Lam, Pannag Sanketi, et al. Openvla: An open-source vision-language-action model. *arXiv preprint arXiv:2406.09246*, 2024.
- Mykel J Kochenderfer. *Decision making under uncertainty: theory and application*. MIT press, 2015.

- Joonho Lee, Jemin Hwangbo, Lorenz Wellhausen, Vladlen Koltun, and Marco Hutter. Learning quadrupedal locomotion over challenging terrain. *Science robotics*, 5(47):eabc5986, 2020a.
- Kimin Lee, Younggyo Seo, Seunghyun Lee, Honglak Lee, and Jinwoo Shin. Context-aware dynamics model for generalization in model-based reinforcement learning. In *International Conference on Machine Learning*, pp. 5757–5766. PMLR, 2020b.
- Jens Lehmann, Robert Isele, Max Jakob, Anja Jentsch, Dimitris Kontokostas, Pablo N Mendes, Sebastian Hellmann, Mohamed Morsey, Patrick Van Kleef, Sören Auer, et al. Dbpedia—a large-scale, multilingual knowledge base extracted from wikipedia. *Semantic web*, 6(2):167–195, 2015.
- Wolfgang Maass. Neural nets with superlinear vc-dimension. *Neural Computation*, 6(5):877–884, 1994.
- Viktor Makoviychuk, Lukasz Wawrzyniak, Yunrong Guo, Michelle Lu, Kier Storey, Miles Macklin, David Hoeller, Nikita Rudin, Arthur Allshire, Ankur Handa, et al. Isaac gym: High performance gpu-based physics simulation for robot learning. *arXiv preprint arXiv:2108.10470*, 2021.
- Leonor Michaelis, Maud L Menten, et al. Die kinetik der invertinwirkung. *Biochem. z*, 49(333-369): 352, 1913.
- Mayank Mittal, Calvin Yu, Qinxu Yu, Jingzhou Liu, Nikita Rudin, David Hoeller, Jia Lin Yuan, Ritvik Singh, Yunrong Guo, Hammad Mazhar, et al. Orbit: A unified simulation framework for interactive robot learning environments. *IEEE Robotics and Automation Letters*, 8(6):3740–3747, 2023.
- Hannes Mühleisen and Christian Bizer. Web data commons-extracting structured data from two large web corpora. *LDOW*, 937(133-145):65, 2012.
- Suraj Nair, Aravind Rajeswaran, Vikash Kumar, Chelsea Finn, and Abhinav Gupta. R3m: A universal visual representation for robot manipulation. In *Conference on Robot Learning*, pp. 892–909. PMLR, 2023.
- Abhishek Padalkar, Acorn Pooley, Ajinkya Jain, Alex Bewley, Alex Herzog, Alex Irpan, Alexander Khazatsky, Anant Rai, Anikait Singh, Anthony Brohan, et al. Open x-embodiment: Robotic learning datasets and rt-x models. *arXiv preprint arXiv:2310.08864*, 2023.
- Xue Bin Peng, Marcin Andrychowicz, Wojciech Zaremba, and Pieter Abbeel. Sim-to-real transfer of robotic control with dynamics randomization. In *2018 IEEE international conference on robotics and automation (ICRA)*, pp. 3803–3810. IEEE, 2018.
- Ilija Radosavovic, Tete Xiao, Bike Zhang, Trevor Darrell, Jitendra Malik, and Koushil Sreenath. Real-world humanoid locomotion with reinforcement learning. *Science Robotics*, 9(89):eadi9579, 2024.
- John Schulman, Filip Wolski, Prafulla Dhariwal, Alec Radford, and Oleg Klimov. Proximal policy optimization algorithms. *arXiv preprint arXiv:1707.06347*, 2017.
- Shai Shalev-Shwartz and Shai Ben-David. *Understanding machine learning: From theory to algorithms*. Cambridge university press, 2014.
- Mohit Shridhar, Lucas Manuelli, and Dieter Fox. Cliport: What and where pathways for robotic manipulation. In *Conference on robot learning*, pp. 894–906. PMLR, 2022.
- Mohit Shridhar, Lucas Manuelli, and Dieter Fox. Perceiver-actor: A multi-task transformer for robotic manipulation. In *Conference on Robot Learning*, pp. 785–799. PMLR, 2023.
- Eduardo D Sontag et al. Vc dimension of neural networks. *NATO ASI Series F Computer and Systems Sciences*, 168:69–96, 1998.
- Nitish Srivastava, Geoffrey Hinton, Alex Krizhevsky, Ilya Sutskever, and Ruslan Salakhutdinov. Dropout: a simple way to prevent neural networks from overfitting. *The journal of machine learning research*, 15(1):1929–1958, 2014.

- Hengkai Tan, Songming Liu, Kai Ma, Chengyang Ying, Xingxing Zhang, Hang Su, and Jun Zhu. Fourier controller networks for real-time decision-making in embodied learning. In *Forty-first International Conference on Machine Learning*, 2024. URL <https://openreview.net/forum?id=nDps3Q8j21>.
- Josh Tobin, Rachel Fong, Alex Ray, Jonas Schneider, Wojciech Zaremba, and Pieter Abbeel. Domain randomization for transferring deep neural networks from simulation to the real world. In *2017 IEEE/RSJ international conference on intelligent robots and systems (IROS)*, pp. 23–30. IEEE, 2017.
- Emanuel Todorov, Tom Erez, and Yuval Tassa. Mujoco: A physics engine for model-based control. In *2012 IEEE/RSJ international conference on intelligent robots and systems*, pp. 5026–5033. IEEE, 2012.
- An Dinh Vuong, Minh Nhat Vu, Hieu Le, Baoru Huang, Binh Huynh, Thieu Vo, Andreas Kugi, and Anh Nguyen. Grasp-anything: Large-scale grasp dataset from foundation models. *arXiv preprint arXiv:2309.09818*, 2023.
- Tobias Weyand, Andre Araujo, Bingyi Cao, and Jack Sim. Google landmarks dataset v2-a large-scale benchmark for instance-level recognition and retrieval. In *Proceedings of the IEEE/CVF conference on computer vision and pattern recognition*, pp. 2575–2584, 2020.
- Baoyuan Wu, Weidong Chen, Yanbo Fan, Yong Zhang, Jinlong Hou, Jie Liu, and Tong Zhang. Tencent ml-images: A large-scale multi-label image database for visual representation learning. *IEEE access*, 7:172683–172693, 2019.
- Fan Xie, Alexander Chowdhury, M De Paolis Kaluza, Linfeng Zhao, Lawson Wong, and Rose Yu. Deep imitation learning for bimanual robotic manipulation. *Advances in neural information processing systems*, 33:2327–2337, 2020.
- Chengyang Ying, Zhongkai Hao, Xinning Zhou, Hang Su, Songming Liu, Dong Yan, and Jun Zhu. Task aware dreamer for task generalization in reinforcement learning. *arXiv preprint arXiv:2303.05092*, 2023.
- Chengyang Ying, Zhongkai Hao, Xinning Zhou, Xuezhou Xu, Hang Su, Xingxing Zhang, and Jun Zhu. Peac: Unsupervised pre-training for cross-embodiment reinforcement learning. *arXiv preprint arXiv:2405.14073*, 2024.
- Zhecheng Yuan, Tianming Wei, Shuiqi Cheng, Gu Zhang, Yuanpei Chen, and Huazhe Xu. Learning to manipulate anywhere: A visual generalizable framework for reinforcement learning. *arXiv preprint arXiv:2407.15815*, 2024.
- Tony Z Zhao, Vikash Kumar, Sergey Levine, and Chelsea Finn. Learning fine-grained bimanual manipulation with low-cost hardware. *arXiv preprint arXiv:2304.13705*, 2023.
- Ziwen Zhuang, Zipeng Fu, Jianren Wang, Christopher Atkeson, Soeren Schwertfeger, Chelsea Finn, and Hang Zhao. Robot parkour learning. *arXiv preprint arXiv:2309.05665*, 2023.
- Brianna Zitkovich, Tianhe Yu, Sichun Xu, Peng Xu, Ted Xiao, Fei Xia, Jialin Wu, Paul Wohlhart, Stefan Welker, Azyaan Wahid, et al. Rt-2: Vision-language-action models transfer web knowledge to robotic control. In *Conference on Robot Learning*, pp. 2165–2183. PMLR, 2023.

A PROOFS

A.1 DETAILS AND PROOF OF THE LEMMA 1

We follow the setting in Crammer & Mansour (2012). First, assume the hypothesis set of policies to grasp a fixed single point is \mathcal{H} and its VC dimension is d . When considering T tasks each represented by a different grasping position, we take the k -shared task classifier (\mathcal{H}_k, g) (Crammer & Mansour, 2012). Here $\mathcal{H}_k = \{h_1, \dots, h_k\} \subseteq \mathcal{H}$ is a subset of \mathcal{H} and g maps each task $t \in \mathcal{T}$ to some $h_i \in \mathcal{H}_k$. Thus the k -shared task classifier hypothesis is defined as $\mathcal{F}_{\mathcal{H},k} = \{f_{\mathcal{H}_k,g} : |\mathcal{H}_k| = k, \mathcal{H}_k \subseteq \mathcal{H}, g : \mathcal{T} \rightarrow K\}$, here $f_{\mathcal{H}_k,g}(\cdot, t) = h_{g(t)}(\cdot)$. Then Crammer & Mansour (2012) has shown that the VC dimension of $\mathcal{F}_{\mathcal{H},k}$ is at most $\mathcal{O}(T \log k + kd \log(Tkd))$.

As we consider \mathcal{H} as the set of neural networks, previous works have shown that the VC dimension of multi-layer neural networks is around the parameters of the neural networks (Maass, 1994; Sontag et al., 1998). Thus $d \gg T$ in our setting and $\mathcal{O}(T \log k + kd \log(Tkd)) \approx \mathcal{O}(kd \log(Tkd))$.

Finally, we consider the task number T . Assume that grasping two points of which the distance below ϵ is similar, we need around $b^3 / \frac{4}{3} \pi \epsilon^3$ points for covering the grasping cube with size $b \times b \times b$. Thus the VC dimension is at most

$$\mathcal{O}(kd \log(Tkd)) = \mathcal{O}(kd \log(\frac{b^3}{\frac{4}{3} \pi \epsilon^3} kd)) = \mathcal{O}(kd \log(\frac{3b^3 kd}{4\pi \epsilon^3})). \quad (5)$$

A.2 PROOF OF THE LEMMA 2

Proof. Firstly, we convert normalized coordinates to pixel coordinates:

$$\begin{aligned} u_{i\text{min(pixel)}} &= u_{i\text{min}} \times W_i \\ v_{i\text{min(pixel)}} &= v_{i\text{min}} \times H_i \\ u_{i\text{max(pixel)}} &= u_{i\text{max}} \times W_i \\ v_{i\text{max(pixel)}} &= v_{i\text{max}} \times H_i \end{aligned}$$

Then, we compute the center of the bounding box in pixel coordinates:

$$\begin{aligned} u_{i\text{center}} &= \frac{u_{i\text{min(pixel)}} + u_{i\text{max(pixel)}}}{2} \\ v_{i\text{center}} &= \frac{v_{i\text{min(pixel)}} + v_{i\text{max(pixel)}}}{2} \end{aligned}$$

These points represent the projections of the sphere's center onto the image planes.

Secondly, for each camera, we back-project the center point into a 3D viewing ray in camera coordinates:

$$\mathbf{d}_i = K_i^{-1} \begin{bmatrix} u_{i\text{center}} \\ v_{i\text{center}} \\ 1 \end{bmatrix}$$

This gives the direction vector \mathbf{d}_i in the camera coordinate system.

Therefore, we can express the sphere center in camera coordinates since the sphere's center lies somewhere along the viewing ray:

$$\mathbf{C}_{i,\text{cam}} = \lambda_i \mathbf{d}_i$$

where $\lambda_i > 0$ is an unknown scalar representing the distance along the ray from the camera center to the sphere's center.

Thirdly, we transform the sphere center from camera coordinates to world coordinates:

$$\mathbf{C} = R_i^\top \mathbf{C}_{i,\text{cam}} + \mathbf{t}_i = R_i^\top (\lambda_i \mathbf{d}_i) + \mathbf{t}_i$$

This must hold true for both cameras:

$$\mathbf{C} = R_1^\top (\lambda_1 \mathbf{d}_1) + \mathbf{t}_1 = R_2^\top (\lambda_2 \mathbf{d}_2) + \mathbf{t}_2$$

By equating the expressions for \mathbf{C} we get:

$$R_1^\top(\lambda_1 \mathbf{d}_1) + \mathbf{t}_1 = R_2^\top(\lambda_2 \mathbf{d}_2) + \mathbf{t}_2$$

By rewriting we have:

$$R_1^\top \mathbf{d}_1 \lambda_1 - R_2^\top \mathbf{d}_2 \lambda_2 = \mathbf{t}_2 - \mathbf{t}_1$$

Let's denote:

$$\begin{aligned} \mathbf{a}_1 &= R_1^\top \mathbf{d}_1 \\ \mathbf{a}_2 &= R_2^\top \mathbf{d}_2 \\ \mathbf{b} &= \mathbf{t}_2 - \mathbf{t}_1 \end{aligned}$$

So the equation becomes:

$$\mathbf{a}_1 \lambda_1 - \mathbf{a}_2 \lambda_2 = \mathbf{b}$$

Note that this is a system of three linear equations with two unknowns λ_1 and λ_2 :

$$\begin{cases} a_{1x} \lambda_1 - a_{2x} \lambda_2 = b_x \\ a_{1y} \lambda_1 - a_{2y} \lambda_2 = b_y \\ a_{1z} \lambda_1 - a_{2z} \lambda_2 = b_z \end{cases}$$

Since we have more equations than unknowns (overdetermined system), we can solve for λ_1 and λ_2 using least squares estimation.

Note that this can be written in matrix form:

$$\begin{bmatrix} a_{1x} & -a_{2x} \\ a_{1y} & -a_{2y} \\ a_{1z} & -a_{2z} \end{bmatrix} \begin{bmatrix} \lambda_1 \\ \lambda_2 \end{bmatrix} = \begin{bmatrix} b_x \\ b_y \\ b_z \end{bmatrix}$$

Let A be the 3×2 matrix of coefficients, $\boldsymbol{\lambda}$ the vector of unknowns, and \mathbf{b} the vector of constants:

$$A = \begin{bmatrix} a_{1x} & -a_{2x} \\ a_{1y} & -a_{2y} \\ a_{1z} & -a_{2z} \end{bmatrix}, \quad \boldsymbol{\lambda} = \begin{bmatrix} \lambda_1 \\ \lambda_2 \end{bmatrix}, \quad \mathbf{b} = \begin{bmatrix} b_x \\ b_y \\ b_z \end{bmatrix}$$

We can compute the least squares solution:

$$\boldsymbol{\lambda} = (A^\top A)^{-1} A^\top \mathbf{b}$$

Once λ_1 and λ_2 are found, \mathbf{C} can be calculated using either camera's equation:

$$\mathbf{C} = R_1^\top(\lambda_1 \mathbf{d}_1) + \mathbf{t}_1$$

Alternatively, we compute both and average them for robustness:

$$\mathbf{C} = \frac{1}{2} (R_1^\top(\lambda_1 \mathbf{d}_1) + \mathbf{t}_1 + R_2^\top(\lambda_2 \mathbf{d}_2) + \mathbf{t}_2)$$

Finally, since λ_i and λ_2 are found, we can compute the distance Z_i from the camera along the viewing direction \mathbf{d}_i :

$$\mathbf{C}_{i,\text{cam}} = \lambda_i \mathbf{d}_i = Z_i \cdot \hat{\mathbf{d}}_i$$

where $\hat{\mathbf{d}}_i$ is normalized by:

$$\hat{\mathbf{d}}_i = \frac{\mathbf{d}_i}{\|\mathbf{d}_i\|}$$

The projected radius of the sphere s_i (in pixels) is half the size of the bounding box width or height (assuming the sphere projects to a circle):

$$s_i = \frac{w_i + h_i}{4}$$

where

$$\begin{aligned} w_i &= u_{i\text{max(pixel)}} - u_{i\text{min(pixel)}} \\ h_i &= v_{i\text{max(pixel)}} - v_{i\text{min(pixel)}} \end{aligned}$$

Consider similar triangles in the imaging geometry:

$$\frac{s_i}{f_i} = \frac{r}{Z_i}$$

We can compute the radius of the sphere:

$$r = \frac{s_i \cdot Z_i}{f_i}$$

Additionally, the solution is unique provided that:

- **The Cameras Are Not Aligned:** The direction vectors \mathbf{a}_1 and \mathbf{a}_2 are not colinear.
- **Non-Degenerate Configuration:** The cameras have different positions or orientations, ensuring the lines of sight intersect at a single point.

Under these conditions, the least squares solution yields a unique λ , and thus unique \mathbf{C} and r .

□

B ABLATION STUDY

To demonstrate the essential role of 3D spatial and 1D temporal information for spatial intelligence, we perform an additional experiment focusing on **temporal variability**, in addition to the spatial generalization tests in Sec. 4. This experiment includes an ablation study comparing models trained on a few selected key timesteps with those trained on all timesteps in a full trajectory. To further illustrate the robust inference capabilities achieved by the enhanced **policy generalization**, we test the policy’s ability to handle significant uncertainty in the output of the visual model. During inference, we apply random masks and noise to the visual model’s bounding box outputs, allowing us to evaluate the policy’s generalization ability under such conditions.

Training with Only Key Steps. To assess the impact of temporal information on policy effectiveness, we conduct an experiment where the model is trained using only key steps from the trajectory. The specific key steps selected were [0, 18, 20, 22, 70], chosen to represent pivotal moments in the trajectory for the grasping task: 0 corresponds to the initial state before the gripper starts approaching the apple, 70 represents the final state when the robotic arm retracts, and steps 18 to 22 denote intermediate states where the gripper makes contact with the apple and closes around it.

Table 2: Success Rates for Training with Only Key Steps

Experiment	Real Robot Success Rate	Simulation Success Rate
Training with Full Trajectory	90%	81.25%
Training with Key Steps	0%	4.17%

The results in Tab. 2 indicate a stark difference in performance between training with the full trajectory and training with only key steps. Training with the full trajectory resulted in a success rate of 90% on the real robot and 81.25% in simulation. In contrast, training with only key steps leads to complete failure on the real robot (0% success rate) and a significantly reduced success rate of 4.17% in simulation. This outcome highlights that relying solely on key steps fails to provide the temporal continuity necessary for effective spatial generalization. The policy’s inability to capture sufficient context from isolated states results in poor action generation and overall task failure.

Different Mask Ratios during Inference. During the inference phase, visual models such as YOLO-World may not always successfully identify objects, leading to significant uncertainty in visual input. To test our policy’s robustness against this visual uncertainty, we introduce masks that randomly obscured bounding box input at varying ratios (0.0 to 1.0).

As shown in Fig. 6, the results reveal that the policy maintains a high success rate and generalization capability when the mask ratio is below 0.4. As the mask ratio exceeds 0.4, the success rate significantly declines, leading to consistent policy failures. This trend reveals that our approach focusing

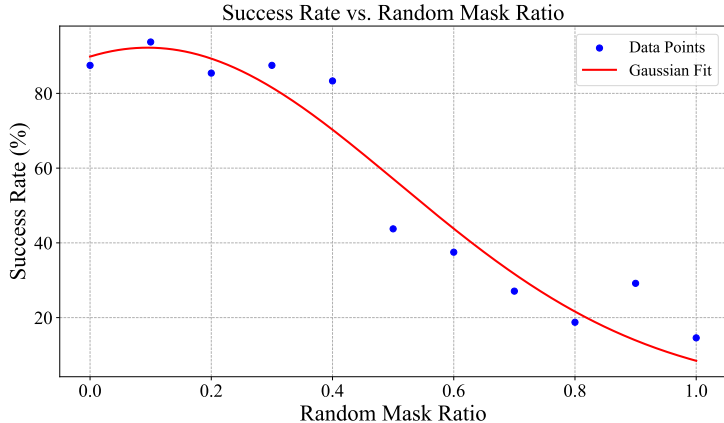


Figure 6: The relationship between random mask ratio and success rate. The fitted curve represents a Gaussian function of $y = 92.23 \exp\left(-\frac{(x-0.09)^2}{2 \cdot 0.41^2}\right)$.

on policy generalizability can resist visual uncertainty up to 40% of the masking ratio. That is, even if 40% of the visual information is lost, the policy still has good spatial generalizability. We fitted the data points with a Gaussian curve to represent this trend, defined by the equation:

$$y(x) = a \cdot e^{-\frac{(x-b)^2}{2c^2}} \quad (6)$$

where a , b , and c are parameters that define the height, center, and width of the curve, respectively. This curve demonstrates that the policy is resilient up to moderate levels of visual masking (mask ratios up to 0.3), but performance degrades significantly as the masking ratio increases beyond 0.4.

This experiment validates that our policy can withstand moderate visual uncertainties during inference, maintaining robust performance. However, the steep decline in success rate for higher mask ratios highlights the importance of reliable visual input for effective spatial reasoning and task execution.

Random Noise in Bounding Boxes. To further examine the policy’s robustness against visual uncertainty, we introduce random noise to the bounding boxes during inference. We tested noise ratios at increments of 0.01, 0.02, 0.05, 0.1, 0.2, and 0.5. Fig. 7 illustrates the success rate as a function of noise ratio, where a monotonic decay fit highlights the policy’s performance trend. The results show that the policy maintains a high success rate at low noise ratios but experienced a significant decrease as noise levels increased. Since our normalized bounding box value ranges from 0 to 1, the policy still achieves a high success rate with a visual detection error of 0.05, demonstrating the robustness of the policy generalization to cope with visual uncertainty and visual sim2real gap.

Our experiments highlight that achieving spatial intelligence requires both continuous temporal information and sufficient spatial data. The experiments in our main text demonstrate that spatial generalizability requires sufficient spatially varying data. The first ablation experiment shows that continuous temporal context is crucial for effective policy performance, while the second and third ablation experiments demonstrate that policy generalization can cope with notable visual uncertainty.

C TEACHER-STUDENT TRAINING DETAILS

C.1 TEACHER POLICY DETAILS

We train our teacher policy using PPO with 8,192 parallel environments in Isaac Lab (Mittal et al., 2023). With a carefully designed reward function and applied PPO techniques, the training is completed in around 40 minutes, reaching approximately 2,000 training iterations.

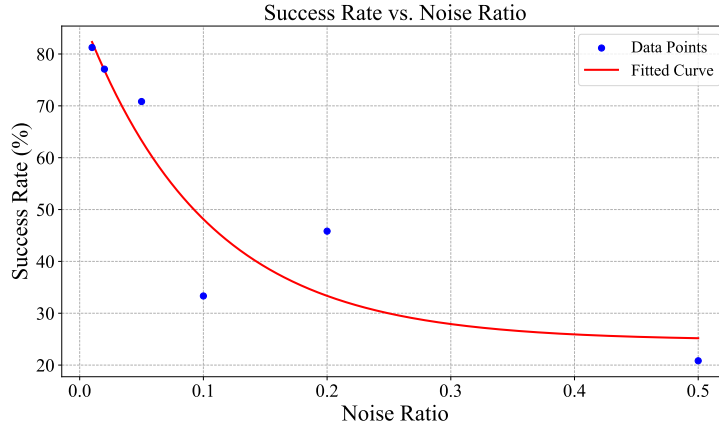


Figure 7: The relationship between random mask ratio and success rate. The fitted curve represents an exponential function of $y = 63.62 \exp(10.01x) + 24.75$.

C.1.1 SIMULATION SCENARIO SETUP

The environment is built based on the lift task in Isaac Lab. During training, the scene consists of a table, an apple, and a robot. To support future extensions to more complex tasks, such as obstacle avoidance during grasping, we represent the robot’s behavior with a 30Hz trajectory. Each environment in the simulator is evenly spaced to prevent interference between different training instances. The apple’s scale is uniformly randomized across environments, while its spatial position and the height of the table are uniformly randomized for each individual run. Further details on the randomized ranges can be found in Table 3.

Table 3: Environment Randomization Parameters

Spatial Range	Table Height (z)	Apple X Position	Apple Y Position
Fix Point	(−0.00, 0.00)	(−0.0, 0.0)	(−0.0, 0.0)
5 cm × 5 cm × 5 cm	(−0.025, 0.025)	(−0.025, 0.025)	(−0.025, 0.025)
10 cm × 10 cm × 10 cm	(−0.07, 0.03)	(−0.05, 0.05)	(−0.05, 0.05)
20 cm × 20 cm × 20 cm	(−0.1, 0.1)	(−0.1, 0.1)	(−0.05, 0.15)
Full Space (41 cm × 30 cm × 28 cm)	(−0.13, 0.15)	(−0.22, 0.08)	(−0.05, 0.36)
Apple 3D Scale Range	((0.77, 0.82), (0.77, 0.82), (0.77, 0.82))		

C.1.2 DETAILS OF OBSERVATION AND ACTION

We provide detailed information about the observations and actions used in training the teacher policy for the multi-environment object-grasping manipulation task:

- **Observations:**
 - Contact forces (24-dimensional)
 - Joint position (8-dimensional)
 - Joint velocity (8-dimensional)
 - Object position (3-dimensional)
 - Target location (7-dimensional)
 - Last action (8-dimensional)
- **Actions:**
 - Joint Position (8-dimensional) (We choose position control. The action is the expected joint position for the next timestep.)

C.1.3 IMPLEMENTATION OF PPO

Our PPO implementation is built on `rsLrL`, and leverages several techniques to improve stability and performance. Key components and their settings are summarized in Table 4.

Table 4: PPO Parameter Settings

Techniques	Parameter	Value
Clipped Surrogate Objective	clip_param	0.2
Value Function Clipping	use_clipped_value_loss	True
Value Loss Coefficient	value_loss_coef	1.0
Adaptive KL Penalty	desired_kl	0.01
Entropy Regularization	entropy_coef	0.01
Generalized Advantage Estimation (GAE)	gamma	0.99
	lam	0.95
Gradient Clipping	max_grad_norm	1.0
Learning Rate	learning_rate	0.001
Mini-Batch	num_mini_batches	4
Learning Epochs	num_learning_epochs	5
Schedule	schedule	adaptive
Empirical Normalization	empirical_normalization	True

C.1.4 REWARD FUNCTION DESIGN

To ensure the policy achieves the desired grasping behavior on our robot, we design a reward function that reflects the task’s objectives. As grasping is complicated, it can be divided into a multi-stage reward function: first reaching the object, then closing the jaws, then picking up the object, and finally retracting the robotic arm to a specified position.

Details of our reward function design for the specific object-grasp tasks can be found in Table 5

Table 5: Reward Function Design

Reward Term	Weight
Fingers Open	5.0
Reaching Object	15.0
Object Goal Tracking	80.0
Object Goal Tracking (Fine-Grained)	70.0
Action Rate Penalty	-1e-4
Joint Velocity Penalty	-1e-4
Contact Forces	10
Close Fingers	100
Lift End Effector (EE)	20
Lift Object	100

C.2 DATA GENERATION DETAILS

In data generation, as shown in Fig. 2, we feed the images from the n_{cam} first-person cameras of the robot to YOLO-World at each timestep to detect the n_{obj} target objects to be manipulated, thus obtaining $n_{cam} * n_{obj}$ bounding boxes. Then we normalize the bounding box, concatenate them, and obtain a vector \mathbf{o} of dimension $4 * n_{cam} * n_{obj}$ as the visual feature input for the control policy. We then store the visual features σ_t^{vis} , all joint positions of the robot σ_t^{rob} , and actions \mathbf{a}_t for each step in the form of trajectories.

To reduce visual interference between parallel environments and minimize the sim-to-real gap, we incorporate a white room during data collection. Three RGB-D cameras¹, calibrated with intrinsic

¹But we only use RGB information.

and extrinsic parameters matching those of the real robot, capture visual information. During inference, the images from these cameras are processed by YOLO-World to generate object bounding boxes.

Table 6: Camera Parameters

Camera	Link	Image Shape and Type
cam_high	fr_link6	Shape: [480, 640, 4] RGB, Range: 0-255 (torch.uint8)
cam_left_wrist	fl_link6	Shape: [480, 640, 4] RGB, Range: 0-255 (torch.uint8)
cam_right_wrist	fr_link6	Shape: [480, 640, 4] RGB, Range: 0-255 (torch.uint8)

Given the high memory demands of image data, we run 16 parallel environments on a single GPU² for data generation, achieving up to 36k successful trajectories per day. For ACT training, these trajectories are subsequently stored in an HDF5 data structure³ (see Table 7). In our approach, we convert images to bounding boxes using YOLO-World and store the results in a dictionary format. Each trajectory consists of multiple steps, with each step containing bbox, qpos, and action data.

Table 7: HDF5 Data Structure

Group/Attribute	Dataset/Attribute Name	Description
Root Attributes	sim	Boolean indicating simulation (False)
	compress	Compression flag from 'CollectEpsBuf'
Datasets	action	Array of actions taken
	reward	Array of rewards received
	base_action	Array of base actions
	base_action_t265	(Optional) Base actions from T265 sensor
Observations: states	qpos	Array of joint positions
	qvel	Array of joint velocities
	effort	Array of joint efforts
Observations: images	cam_high	Byte-encoded images from 'cam_high'
	cam_left_wrist	Byte-encoded images from 'cam_left_wrist'
	cam_right_wrist	Byte-encoded images from 'cam_right_wrist'

C.3 STUDENT POLICY DETAILS

We use RNN and ACT to train our student policy. The details of training parameters can be found in Table 8 and Table 9.

D HARDWARE DETAILS

The robot is equipped with a dual-arm design, providing a total of 14 degrees of freedom (DoF), with 7 DoF per arm for versatile movement. Each arm has a maximum valid payload of 1500g, and the gripper has a range of up to 80mm, allowing the robot to perform a variety of grasping and manipulation tasks efficiently. The detailed hardware information and an image of the robot can be found in Figure 8 and Table 10.

²For some 24 GB GPU.

³Video-based dataset

Table 8: RNN Training Parameters

Parameter	Value
lr	0.002
lr_backbone	7e-05
epochs	50
warmup_ratio	0.1
use_scheduler	cos
weight_decay	0.0001
loss_function	l1
hidden_dim	512
rnn_layers	3
rnn_hidden_dim	512
actor_hidden_dim	512
policy_class	RNN
gradient_accumulation_steps	1
random_mask_ratio	0.3

Table 9: ACT Training Parameters

Parameter	Value
num_epochs	1000
lr	4e-05
lr_backbone	7e-05
weight_decay	0.0001
kl_weight	10
backbone	resnet18
position_embedding	sine
loss_function	l1
chunk_size	32
hidden_dim	512
dim_feedforward	3200
enc_layers	4
dec_layers	7
nheads	8
dropout	0.2
train_loader_len	23
warmup_ratio	0.1
scheduler	cosine

E EXPERIMENTAL DETAILS

We test the success rate of student policy in both simulator and real world.

E.1 EVALUATION IN SIMULATION

We run large-scale experiments in simulator to test the spatial generalization curve for each range and determine the minimum data amounts to achieve optimal success rate. To align with real machine inference, we set robot’s joints directly to target qpos instead of using environment stepping. We mark the trajectory as success if there is a step both reaching reward > 0.6 and quat reward > 1.4 . For each policy, we test 48 trajectories and record the final success rate.

E.2 EXPERIMENT RESULT ANALYSIS

We discuss here the analysis of the results of spatial scaling law.

Parameter	Value
Size	1080 × 700 × 1140
Arm weight	4.2 kg
Arm Payload	3000 g (peak) 1500 g (valid)
Arm reach	600 mm
Arm repeatability	1 mm
Arm working radius	653 mm
Joint motion range	J1: ±154°, J2: 0°~165° J3: -175°~0°, J4: ±106° J5: ±75°, J6: ±100°
Gripper range	0-80 mm
Gripper max force	10 NM
DoF	7 × 2 = 14

Table 10: Technical specifications.

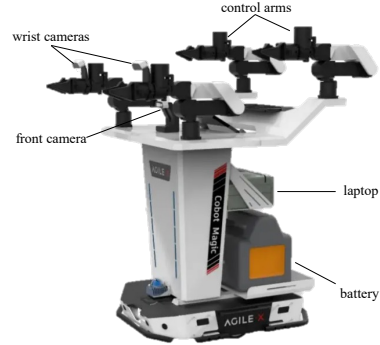


Figure 8: Hardware features.

By fitting the resulting data points, we observe that as the training data increases, the success rate of the policies quickly rises and eventually converges to an upper bound, which aligns well with the form of the Michaelis-Menten (Michaelis et al., 1913) equation:

$$\text{success_rate} = \frac{V_{\max} \times \text{num_traj}}{K_m + \text{num_traj}} \quad (7)$$

where V_{\max} represents the maximum achievable success rate, and K_m is the number of trajectories at which the success rate is half of V_{\max} . This equation captures the saturation-type growth observed in the policy performance.

across different settings, the amount of data required to achieve an 80% success rate shows a power function as the data increases:

$$\text{data_volume} = 1507 \cdot \text{spatial_volume}^{0.28} \quad (8)$$

For the functional relationship between the amount of data required for spatial generalization and spatial volume, we explored two types of fits: a power law and a logarithmic function. The fitting results of power law is given by $y = a \cdot x^b = 1507x^{0.28}$, while the logarithmic fit is $y = a \cdot \ln(b \cdot x) + c = 2450.69 \cdot \ln(0.51 \cdot x) - 1604.28$. We found that the logarithmic fit becomes unreasonable as the spatial volume x approaches 0, where the required data, $y = 2450.69 \cdot \ln 0.51 \cdot x - 1604.28$, tends to negative infinity, which is unrealistic since the amount of data cannot be negative. Furthermore, the fit results in a negative value at $x = 2$, where $bx = 1$ and $\log(bx) = 0$, leading to a required data amount of $a \log(bx) + c = -1604$. In the long run (for larger spatial volumes), the power law fit better describes the relationship between the data required for spatial generalization and spatial volume. Fig. 9 shows the selected power law relationship, and Fig. 10 displays the logarithmic curve.

E.3 EVALUATION IN REAL WORLD

To verify our experiment results from simulator, we also test our policy in real robot. For each range, we choose the first optimal policy that achieves 80% success rate in simulator and evaluate with real machine for 10 randomly chosen points.

In addition to the verification of spatial generalization, we also test the ability of object, background, and complex generalizations. The details of experiment setting can be found in Table 11.

The three camera images, as well as the entire trajectory of grasping, are schematized below:

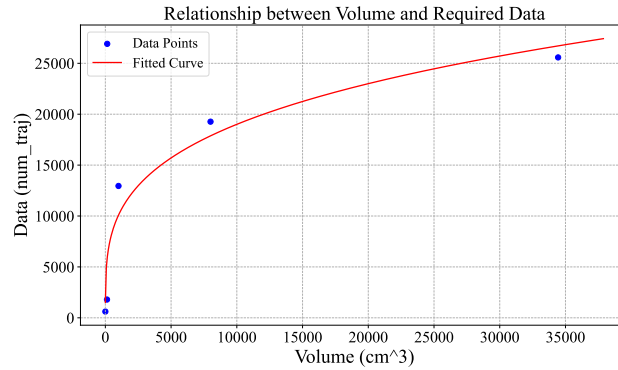


Figure 9: Demonstration of the power-rate relationship between spatial volume and data amounts needed to reach 80% success rate in the grasping task.

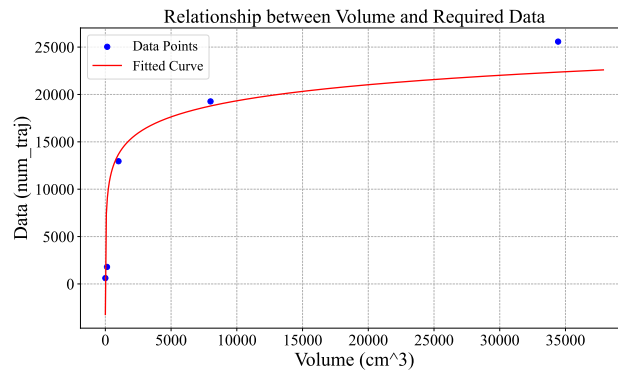


Figure 10: Demonstration of the logarithmic relationship between spatial volume and data amounts needed to reach 80% success rate in the grasping task.

Table 11: Real-World Experiment Settings

Generalization Type	Setting Description
Object Generalization	
Yellow Pear	h4: Point Random, Minimal setting
Orange	h4: Point Random, Minimal setting
Steel Cup	h4: Point Random, Minimal setting
Tin Can	h4: Point Random, Minimal setting
Glass Beaker	h4: Point Random, Minimal setting
Background Generalization	
Apple	h4: Point Random, Orange tablecloth
Unseen Apple	h4: Point Random, Black tablecloth
Apple	h4: Point Random, Playing video
Apple	h4: Point Random, Dim light
Apple	h4: Point Random, Flittering light
Complex Generalization	
Unseen Apple, Unseen Table	Point Random, Table 2
Unseen Apple, Unseen Desk	Point Random, Multiple objects
Steel Cup, Unseen Desk	Point Random, Daily desktop
Plastic Bottle, Unseen Desk	Point Random, Daily desktop

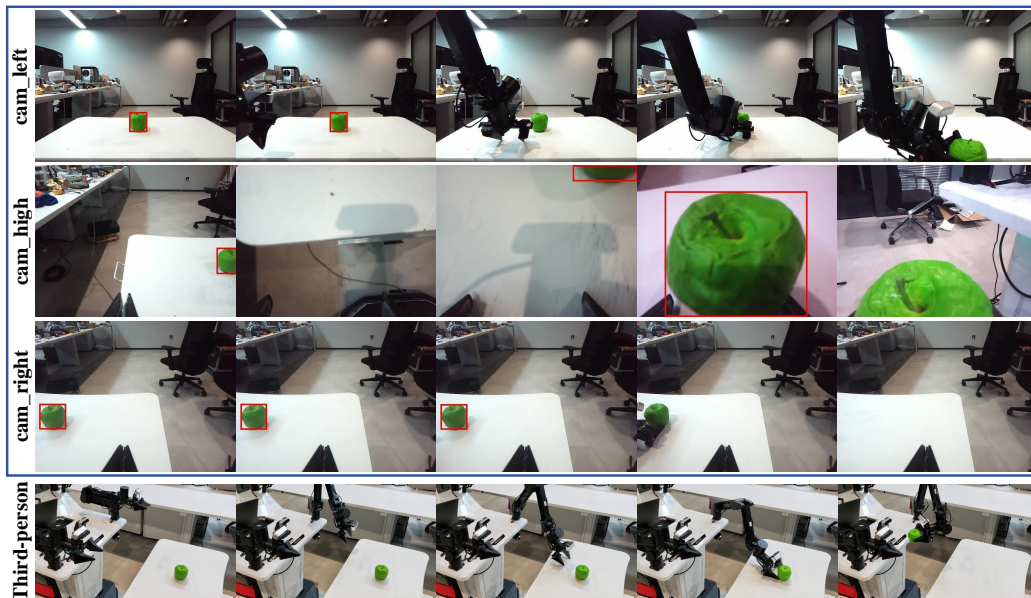


Figure 11: Pictures of the entire trajectory of grasping, including perspective and three camera views.